Research Article | Open Access

Chemical Synthesis

Cui *et al. Chem. Synth.* **2026**, *6*, 29 **DOI:**10.20517/cs.2025.91

Porous aromatic frameworks by highly connected building blocks for hydrogen and methane storage

Lei Cui[1,#], Mengzhen Zhang[1,#], Qihaoyue Wang[1,#], Danyang Feng[1], Lin Lin[1], Zihao Wang[1], Jianfeng Liu[2], Jiangtao Jia[1,*], Zheng Bian[1,*], Bao-Lian Su[3,4,5,*], Guangshan Zhu[1,*]

Keywords:
Porous aromatic frameworks, topology-guided synthesis strategy, hydrogen storage, methane storage

Citation: Cui, L.; Zhang, M.; Wang, Q.; Feng, D.; Lin, L.; Wang, Z.; Liu, J.; Jia, J.; Bian, Z.; Su, B. L.; Zhu, G. Porous aromatic frameworks by highly connected building blocks for hydrogen and methane storage. *Chem. Synth.* **2026**, *6*, 29. https://dx.doi.org/10.20517/cs.2025.91

Received: 21 Aug 2025 **First Decision:** 2 Sep 2025 **Revised:** 20 Sep 2025 **Accepted:** 25 Sep 2025 **Published:** 12 Mar 2026

Academic Editor: Xiaoxin Zou
Copy Editor: Pei-Yun Wang
Production Editor: Pei-Yun Wang

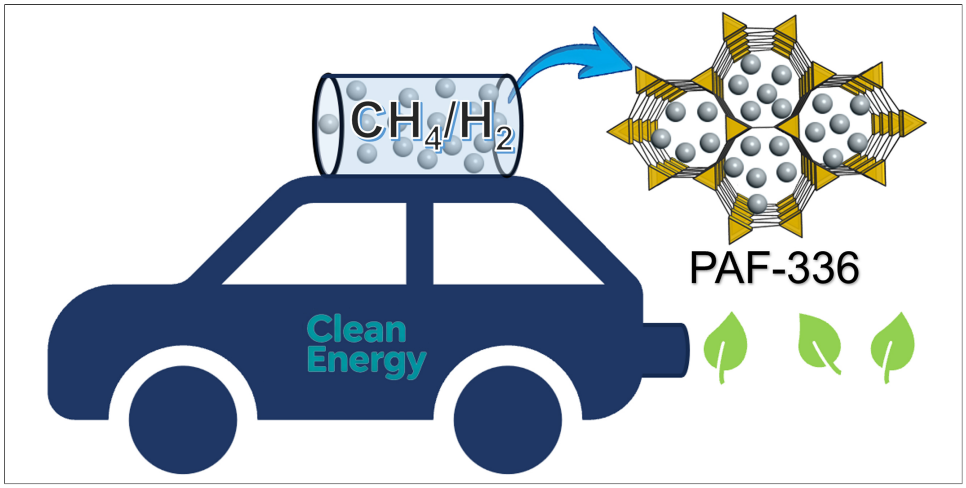

Abstract

The fabrication of porous materials possessing ultrahigh specific surface areas remains a significant challenge. We report the synthesis of two novel porous aromatic frameworks, PAF-336 and PAF-337, constructed from 6- and 8-connected building blocks with triangular prismatic and cuboid geometries, respectively. PAF-336 demonstrates an ultrahigh specific surface area (~5,210 $m^2 \cdot g^{-1}$) and large pore volume (3.5 $cm^3 \cdot g^{-1}$). This high porosity translates to high hydrogen storage capacity and state-of-the-art methane storage performance, positioning PAF-336 as a potential material for clean energy storage.

[1]Key Laboratory of Polyoxometalate and Reticular Material Chemistry of the Ministry of Education, Faculty of Chemistry, Northeast Normal University, Changchun 130024, Jilin, China.
[2]Analysis Lab, Beishide Instrument Technology (Beijing) Co., Ltd., Beijing 100006, China.
[3]Laboratory of Inorganic Materials Chemistry (CMI), University of Namur, Namur B-5000, Belgium.
[4]State Key Laboratory of Advanced Technology for Materials Synthesis and Processing, Wuhan University of Technology, Wuhan 430070, Hubei, China.
[5]Clare Hall, University of Cambridge, Cambridge CB2 1EW, UK.
[#]These authors contribute equally to this paper.

***Correspondence to:** Prof. Jiangtao Jia, Prof. Zheng Bian, Prof. Guangshan Zhu, Key Laboratory of Polyoxometalate and Reticular Material Chemistry of the Ministry of Education, Faculty of Chemistry, Northeast Normal University, Changchun 130024, Jilin, China. E-mail: jiangtaojia@nenu.edu.cn; bianz070@nenu.edu.cn; zhugs@nenu.edu.cn; Prof. Bao-Lian Su, Laboratory of Inorganic Materials Chemistry (CMI), University of Namur, Namur B-5000 Belgium. E-mail: bao-lian.su@unamur.be

INTRODUCTION

Carbon dioxide (CO_2) emissions are the main contributor to the critical rise in global temperatures[1-6], primarily caused by the burning of fossil fuels, such as coal and gasoline[7]. Hydrogen (H_2), when used as an energy carrier, produces no CO_2 emissions upon combustion, whereas methane (CH_4) emits significantly less CO_2 than traditional fossil fuels, thereby potentially mitigating the greenhouse effect[8,9]. The main challenge limiting the use of H_2 or CH_4 as energy lies in the storage methods. Currently, the predominant techniques for storing combustible gases involve liquefaction and compression, both of which require costly storage systems and high pressures (typically 250 bar for CH_4 and 700 bar for H_2)[10-12]. In contrast to alternative approaches, porous materials with high specific surface areas and designable topological structure show exceptional promise for H_2 and CH_4 storage[3,13-19].

The pursuit of ultra-high porosity has always been the primary challenge in the design and synthesis of porous materials[20]. Frameworks connected by robust covalent bonds[21-27] are stable and have been demonstrated to be suitable for H_2 and CH_4 storage. Nevertheless, the covalently connected frameworks with ultra-high specific surface area are still quite rare. Notably, diamond structure mimetic porous aromatic framework PAF-1 achieves an ultrahigh Brunauer-Emmett-Teller (BET) surface area (5,600 $m^2 \cdot g^{-1}$) with extraordinary chemical-thermal stability[28]. Subsequent frameworks with ultra-high porosity using tetrahedron-related building blocks were also reported[29-33]. It is well known that the pore size, pore shape and pore environment are related to the H_2 and CH_4 storage performance[10,34,35]. Therefore, developing topology-guided novel building blocks is an effective way to synthesize porous materials with ultrahigh porosity, which will provide new insights for gas storage.

The **acs** [(3,6)-connected net] and **bcu** (8-connected body-centered cubic net) topologies, constructed from highly connected trigonal prismatic and cuboidal building blocks, are both edge-transitive topologies widely used in the design of metal-organic frameworks (MOFs) and covalent organic frameworks (COFs)[36-45]. Herein, we synthesized PAF-336 and PAF-337 targeting **acs** and **bcu** topologies using unprecedented HBPT [2,3,6,7,14,15-hexa(4′-bromophenyl)triptycene] and DMOBPP [6,13-dimethoxy-2,3,9,10,18,19,24,25-octa(4′-bromophenyl)pentiptycene] as monomers through Yamamoto-type coupling reaction [Schemes 1 and 2]. To be noted, PAF-336 presents an extremely high BET surface area of ~5,210 $m^2 \cdot g^{-1}$ and a large pore volume of 3.5 $cm^3 \cdot g^{-1}$, showing significantly high H_2 and CH_4 storage performance.

EXPERIMENTAL

Materials

The chemicals used in this study include: 2,3,6,7,14,15-hexabromotriptycene (HBT, Alfa, > 97%), (4-(trimethylsilyl)phenyl)boronic acid (Macklin, 98%), N-chlorosuccinimide (NCS, Energy Chemical, 98%), tris(dibenzylideneacetone)dipalladium(0) [$Pd_2(dba)_3$, Energy Chemical, 98%], tri-tert-butylphosphine tetrafluoroborate [$HP(tBu)_3BF_4$, Energy Chemical, 98%], sodium dithionite [$Na_2S_2O_4$, Energy Chemical, analytical reagent (AR) grade, ≥ 88.0%], tetra-chloro-1,4-benzoquinone (Energy Chemical, 97%), anthracene (Innochem, 99%), iodomethane (Innochem, 99%), 18-Crown-6 (Macklin, 99%), p-benzoquinone (Macklin, 99%), 1,5-cyclooctadiene (COD, Innochem, 98%), bis(1,5-cyclooctadiene)nickel(0) [$Ni(COD)_2$, Laajoo, 97%], 2,2′-bipyridyl (Aldrich, 99%), N,N-dimethylformamide [DMF, Macklin, 99.8%, with molecular sieves, Water ≤ 50 parts per million (ppm)], and tetrahydrofuran (THF, Macklin, 99.5%, with molecular sieves, Water ≤ 50 ppm). All of the reagents were available commercially and obtained with a high level of purity, obviating the need for additional purification steps.

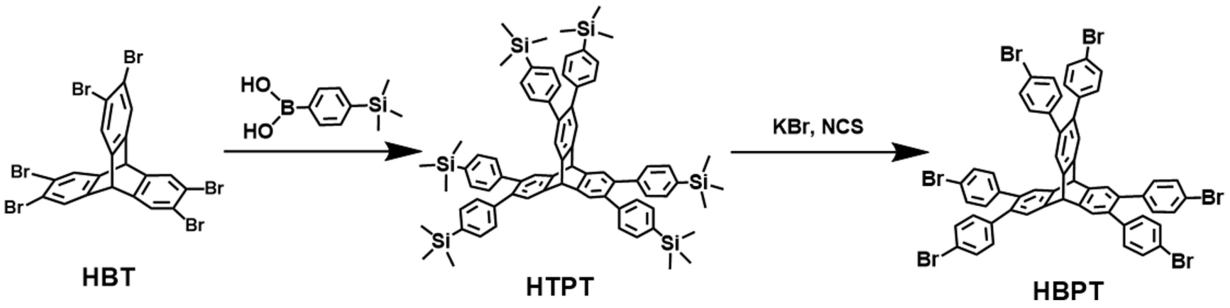

Scheme 1. Synthesis route of HBPT. HBPT: 2,3,6,7,14,15-Hexa(4′-bromophenyl)triptycene; HBT: 2,3,6,7,14,15-hexabromotriptycene; HTPT: 2,3,6,7,14,15-hexa(4′-(trimethylsilyl)phenyl)triptycene; NCS: N-chlorosuccinimide.

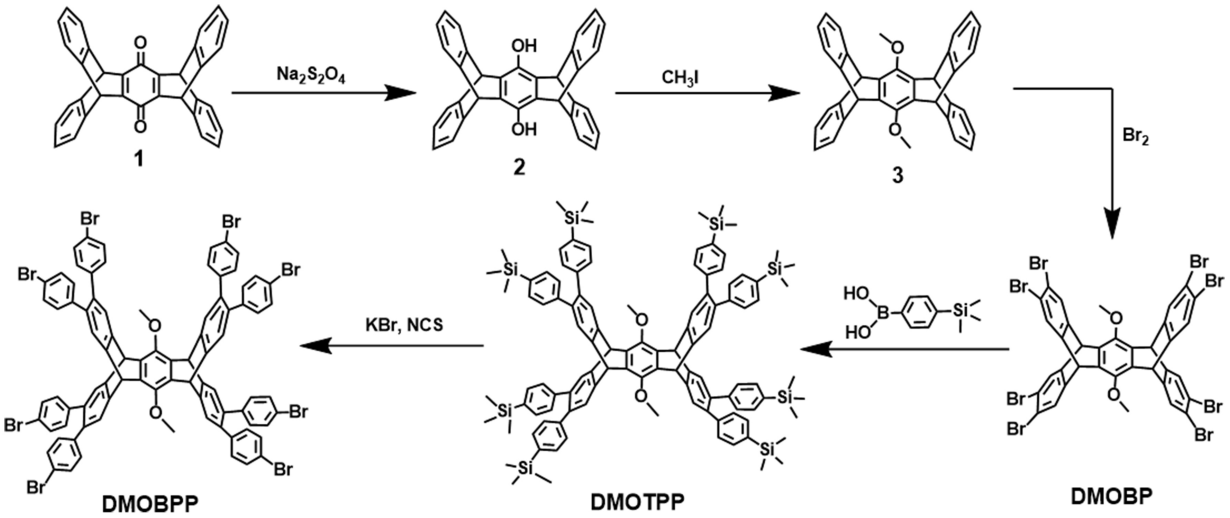

Scheme 2. Synthesis route of DMOBPP. DMOBPP: 6,13-Dimethoxy-2,3,9,10,18,19,24,25-octa(4′-bromophenyl)pentiptycene; DMOBP: 6,13-dimethoxy-2,3,9,10,18,19,24,25-octabromopentiptycene; DMOTPP: 6,13-dimethoxy-2,3,9,10,18,19,24,25-octa(4′-(trimethylsilyl)phenyl)pentiptycene; NCS: N-chlorosuccinimide.

Synthesis method

Synthesis of HBPT

Synthesis of 2,3,6,7,14,15-hexa(4′-(trimethylsilyl)phenyl)triptycene (HTPT)

A combination of HBT (250 mg, 0.34 mmol) and (4-(trimethylsilyl)phenyl)boronic acid (1.00 g, 5.2 mmol) was added to a mixed solvent of anhydrous THF (7 mL) and degassed 1 M aqueous (aq.) K_2CO_3-solution (8 mL). The solution was deoxygenated three times by a freeze-pump-thaw procedure. Under Ar atmosphere, $Pd_2(dba)_3$ (37.8 mg, 0.0413 mmol) and $HP(tBu)_3BF_4$ (29.9 mg, 0.103 mmol) were added quickly, and the mixture was heated at 80 °C with magnetic stirring at 500 rpm for 22 h. After cooling to room temperature, the reaction mixture was diluted with ethyl acetate (20 mL) and the phases were separated. The organic layer was subsequently washed with saturated NH_4Cl aq. solution, water, and brine. After drying over anhydrous magnesium sulfate ($MgSO_4$), the solution was evaporated under reduced pressure, affording the crude product as a primrose yellow solid. After dispersing in methanol, sonication and filtration, the product was washed with MeOH and dried at 80 °C to give HTPT [2,3,6,7,14,15-hexa(4′-(trimethylsilyl)phenyl)triptycene] as a white powder (340 mg, 90% yield). The ^{1}H nuclear magnetic resonance (NMR) and ^{13}C NMR (deuterated chloroform, $CDCl_3$) spectra were shown in Supplementary Figures 1 and 2. ^{1}H NMR (500 MHz, $CDCl_3$) δ (ppm): 7.51 (s, 6 H), 7.31 (d, 12 H), 7.06 (d, 12 H), 5.80 (s, 2 H), 0.21 (s, 27 H). ^{13}C NMR (126 MHz, $CDCl_3$) (ppm): 144.27, 141.96, 138.16, 137.86, 132.95, 129.40, 126.30, 53.35, -0.95.

Synthesis of HBPT

A mixture of HTPT (200 mg, 0.18 mmol) and potassium bromide (KBr, 226 mg, 1.90 mmol) was dissolved in a mixed solvent of CH_3COOH (30 mL) and CH_3OH (4 mL). The solution was heated at 60 °C for 40 min, followed by the addition of NCS (202 mg, 1.50 mmol), after which stirring at 500 rpm was continued for 24 h. After cooling to room temperature, 200 mL of H_2O and 100 mL of dichloromethane (CH_2Cl_2) were added. The organic phase was separated, washed successively with 3 M HCl, aq. NH_3, and water, and dried over anhydrous $MgSO_4$. After solvent removal, the crude product was washed extensively with n-hexane and methanol to afford the pure product as a white powder (177 mg, 83% yield). The ^{1}H NMR and ^{13}C NMR ($CDCl_3$) spectra were shown in Supplementary Figures 3 and 4. The molecular weight was measured as 1,183.8 g·mol^{-1} by matrix-assisted laser desorption/ionization (MALDI) mass spectrometry [Supplementary Figure 5], consistent with the calculated value. ^{1}H NMR (500 MHz, $CDCl_3$) δ (ppm): 7.49 (s, 6 H), 7.32 (d, 12 H), 6.92 (d, 12 H), 5.64 (s, 2 H). ^{13}C NMR (126 MHz, $CDCl_3$) (ppm): 144.42, 139.97, 136.79, 131.59, 131.44, 126.19, 121.19, 53.12.

Synthesis of DMOBPP

Synthesis of Compound 1

A mixture of anthracene (3.02 g, 17 mmol), p-benzoquinone (919 mg, 8.5 mmol) and tetra-chloro-1,4-benzoquinone (4.18 g, 17 mmol) was dissolved in glacial acetic acid (AcOH, 250 mL) and refluxed at 120 °C with magnetic stirring at 500 rpm for 24 h. After cooling to room temperature, the resulting precipitate was collected by filtration. The residue was washed several times with diethyl ether and dried under reduced pressure at room temperature to afford **Compound 1** as a yellow solid (3.5 g, 90% yield). The structure was confirmed using ^{1}H NMR (500 MHz, $CDCl_3$, Supplementary Figure 6). ^{1}H NMR δ (ppm): 7.35 (d, 8 H), 6.96 (d, 8 H), 5.76 (s, 4 H).

Synthesis of Compound 2

Compound 1 (414 mg, 0.90 mmol) and sodium bicarbonate (1.00 g, 12.0 mmol) were dissolved in anhydrous DMF (9 mL), followed by the addition of $Na_2S_2O_4$ (1.00 g, 6 mmol). The mixture was stirred at 500 rpm and 100 °C for 16 h. After cooling, the reaction mixture was poured into water (50 mL). The resulting white precipitate, **Compound 2**, was collected by filtration, washed three times with water, and dried under vacuum at 80 °C for 24 h (400 mg, 96% yield). The structure was confirmed by ^{1}H NMR (500 MHz, $CDCl_3$, Supplementary Figure 7). ^{1}H NMR δ (ppm): 8.01 (s, 2 H), 7.31 (dd, 8 H), 6.91 (dd, 8 H), 5.66 (s, 4 H).

Synthesis of Compound 3

A mixture of **Compound 2** (790 mg, 1.70 mmol), freshly dehydrated K_2CO_3 (1.20 g, 8.70 mmol) and 18-crown-6 (5 mg) was suspended in anhydrous acetone (75 mL), followed by the addition of iodomethane (1.1 mL, 18 mmol). The mixture was stirred at 500 rpm and 70 °C for 14 h and then concentrated under reduced pressure using a rotary evaporator. The resulting residue was dissolved in chloroform ($CHCl_3$) and washed with saturated brine. The organic layer was dried over anhydrous $MgSO_4$, filtered, and concentrated under vacuum. The crude material was purified by column chromatography (gradient elution: 25% to 50% CH_2Cl_2 in hexanes) and dried under vacuum at 60 °C for 24 h to afford **Compound 3** as a white powder (670 mg, 80% yield). The ^{1}H NMR spectrum ($CDCl_3$) is shown in Supplementary Figure 8. ^{1}H NMR (500 MHz, $CDCl_3$) δ (ppm): 7.32 (dd, 8 H), 6.93 (dd, 8 H), 5.67 (s, 4 H), 3.88 (s, 6 H).

Synthesis of 6,13-dimethoxy-2,3,9,10,18,19,24,25-octabromopentiptycene (DMOBP)

Compound 3 (490 mg, 1 mmol) and a catalytic amount of iron filings (50 mg) were added in anhydrous CH_2Cl_2 (56 mL) in a flame-dried 100 mL Schlenk flask. The reaction flask was deoxygenated via three freeze-pump-thaw cycles. After stirring at 500 rpm for 5 min to ensure the complete dissolution of

Compound 3, bromine (Br_2, 0.44 mL, 8.4 mmol) was added. The flask was then subjected to one cycle of evacuation and nitrogen backfilling. After refluxing at 60 °C for 2 h, the reaction mixture was cooled and slowly added into ethanol (40 mL). The resulting yellow precipitate was collected by filtration and purified by recrystallization from a mixture of $CHCl_3$ and ethanol to afford **DMOBP** (867 mg, 78% yield). The ^{1}H NMR spectrum ($CDCl_3$) is shown in Supplementary Figure 9. ^{1}H NMR (500 MHz, $CDCl_3$) δ (ppm): 7.58 (s, 8 H), 5.54 (s, 4 H), 3.86 (s, 6 H).

Synthesis of 6,13-dimethoxy-2,3,9,10,18,19,24,25-octa(4′-(trimethylsilyl)phenyl)pentiptycene (DMOTPP)
A mixture of 6,13-dimethoxy-2,3,9,10,18,19,24,25-octabromopentiptycene (DMOBP, 200 mg, 0.180 mmol) and (4-(trimethylsilyl)phenyl)boronic acid (1.38 g, 7.13 mmol) was dissolved in a mixture of anhydrous THF (18 mL) and degassed 1 M aq. K_2CO_3-solution (24 mL). The resulting mixture was deoxygenated via three freeze-pump-thaw cycles. Under Ar atmosphere, $Pd_2(dba)_3$ (52.2 mg, 0.057 mmol) and $HP(tBu)_3BF_4$ (41.3 mg, 0.14 mmol) were added rapidly, and the mixture was heated at 80 °C with magnetic stirring at 500 rpm for 24 h. After cooling to room temperature, the mixture was extracted with ethyl acetate (50 mL). The organic layer was washed with saturated aq. NH_4Cl, H_2O and brine, then dried by anhydrous $MgSO_4$. After removal of the solvent under reduced pressure, the residue was purified by washing with a large amount of methanol and dried under vacuum at 60 °C for 24 h to afford **DMOTPP** as a yellow precipitate (214 mg, 71% yield). The structure was confirmed with ^{1}H NMR ($CDCl_3$, Supplementary Figure 10). ^{1}H NMR (500 MHz, $CDCl_3$) δ (ppm): 7.46 (s, 8 H), 7.29 (d, 16 H), 7.01 (d, 16 H), 5.84 (s, 4 H), 3.93 (s, 6 H), 0.21 (s, 72 H).

Synthesis of DMOBPP
A mixture of 6,13-dimethoxy-2,3,9,10,18,19,24,25-octa(4′-(trimethylsilyl)phenyl)pentiptycene (DMOTPP, 200 mg, 0.12 mmol) and KBr (307 mg, 2.58 mmol) was dissolved in a solvent mixture of CH_3COOH (45 mL) and CH_3OH (6 mL). the solution was heated at 60 °C with magnetic stirring at 500 rpm for 40 min, followed by the addition of NCS (275.8 mg, 2.07 mmol) in one portion. The resulting mixture was stirred at the same temperature for 24 h. After cooling to room temperature, the reaction was quenched with H_2O (200 mL) and extracted with CH_2Cl_2 (100 mL). The organic phase was separated, washed sequentially with 3 mol/L HCl, aq. NH_3 and H_2O, and then dried with anhydrous $MgSO_4$. After removal of the solvent under reduced pressure, the crude product was purified by washing with copious amounts of n-hexane and methanol to afford **DMOBPP** as a yellow powder (176 mg, 85% yield). The ^{1}H NMR and ^{13}C NMR ($CDCl_3$) spectra were provided in Supplementary Figures 11 and 12. The molecular weight was measured as 1,729.7 g·mol^{-1} by MALDI mass spectrometry [Supplementary Figure 13], consistent with the calculated value. ^{1}H NMR (500 MHz, $CDCl_3$) δ (ppm): 7.42 (s, 8 H), 7.30 (d, 16 H), 6.86 (d, 16 H), 5.86 (s, 4 H), 3.95 (s, 6 H). ^{13}C NMR (126 MHz, $CDCl_3$) (ppm): 147.60, 144.99, 140.13, 136.94, 136.64, 131.81, 131.66, 126.25, 121.44, 63.68, 47.94.

Synthesis of PAF-336 and PAF-337
$Ni(COD)_2$ (1.96 mmol, 538 mg), 2,2′-bipyridyl (1.96 mmol, 306 mg), and COD (2.04 mmol, 0.251 mL) were successively added to dehydrated DMF (20 mL) under a nitrogen atmosphere. The mixture was heated at 80 °C with magnetic stirring at 500 rpm for 1 h to form the catalyst complex, followed by the dropwise addition of a solution of HBPT (300 mg, 0.253 mmol) in dehydrated DMF (10 mL). After stirring at 80 °C for 72 h, the reaction mixture was cooled to room temperature and treated with 6 M HCl (30 mL) for 3 h to remove the nickel species. The resulting solid was collected by filtration and washed with water, methanol, and THF. The white precipitate was dried under vacuum at 120 °C to afford **PAF-336** (165 mg, 92% yield). **PAF-337** (185 mg, 91% yield) was prepared following the same procedure, replacing HBPT (300 mg) with DMOBPP (324 mg).

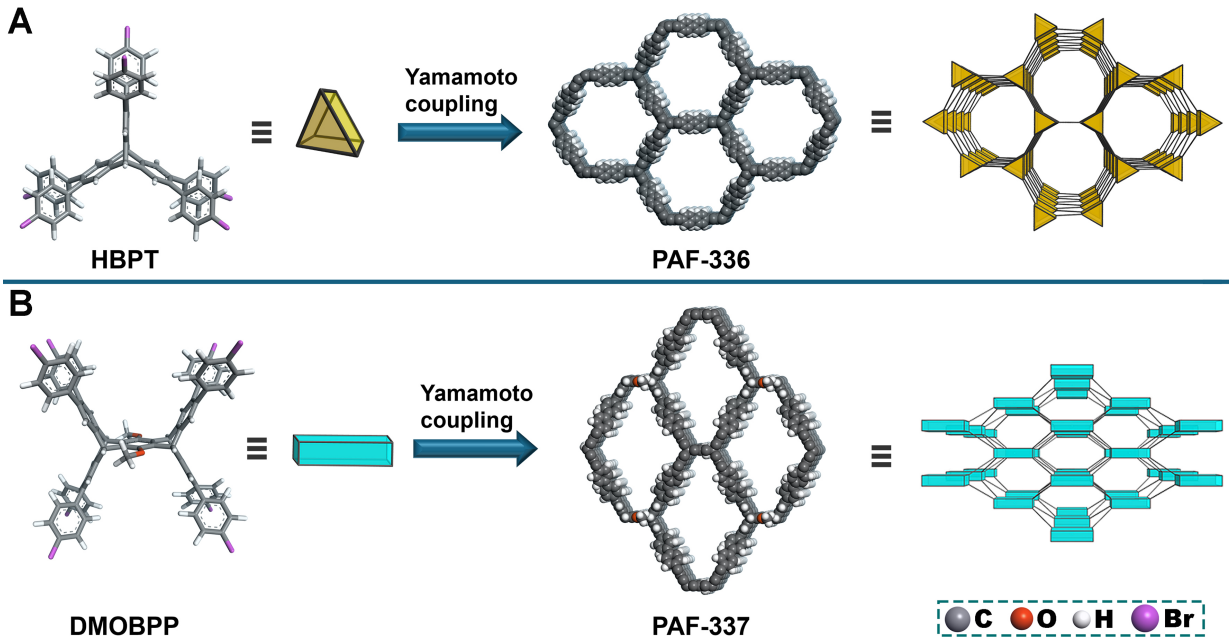

Scheme 3. Topology-guided structural design and simulations of (A) PAF-336 and (B) PAF-337. HBPT: 2,3,6,7,14,15-Hexa(4′-bromophenyl)triptycene; DMOBPP: 6,13-dimethoxy-2,3,9,10,18,19,24,25-octa(4′-bromophenyl)pentiptycene.

Characterizations

The manufacturer, model, and country of origin of the experimental instruments have been provided in the Supplementary Materials.

RESULTS AND DISCUSSION

Simulation and characterization of PAFs

Computational modeling can be employed to predict pore aperture and evaluate the structural feasibility of porous materials. Therefore, the anticipatory frameworks for PAF-336 (based on **acs** topology) and PAF-337 (based on **bcu** topology) were constructed and validated using Material Studio software [Scheme 3]. Computational simulations revealed distinct pore volumes and pore geometries between the two topological frameworks. PAF-336 exhibited a pore volume of 3.5 $cm^3 \cdot g^{-1}$ and featured hexagonal pores approximately 2.2 nm in size. In contrast, PAF-337 had a lower pore volume (2.2 $cm^3 \cdot g^{-1}$) and contained elongated hexagonal pores measuring approximately 2.4 nm × 1.2 nm. Guided by the simulated structure, two bromine-terminated monomers (HBPT and DMOBPP) were strategically designed and synthesized. Notably, the synthesis of monomer DMOBPP involves multiple steps compared to the relatively straightforward synthesis of HBPT, which may pose challenges for the large-scale production and practical application of PAF-337. These monomers served as building blocks for the subsequent preparation of PAF-336 and PAF-337 via Yamamoto-type cross-coupling reaction.

Initially, the monomers of HBPT and DMOBPP were successfully synthesized and structurally characterized [Schemes 1 and 2]. Their chemical identity and purity were rigorously confirmed through ^{1}H NMR and ^{13}C NMR spectroscopy [Supplementary Figures 1-4 and Supplementary Figures 6-12], followed by definitive validation via MALDI mass spectrometry [Supplementary Figures 5 and 13]. The completion of the reaction between the monomers was monitored using Fourier transform-infrared (FT-IR) spectroscopy. As shown in Figure 1A and B [Supplementary Figures 14 and 15], the C-Br peak at 1,070 cm^{-1} disappeared after the reaction, signaling the successful synthesis of PAF-336 and PAF-337 via a C-C coupling reaction[33]. High-resolution X-ray photoelectron spectroscopy (XPS) analysis of the monomers and resulting PAF-336

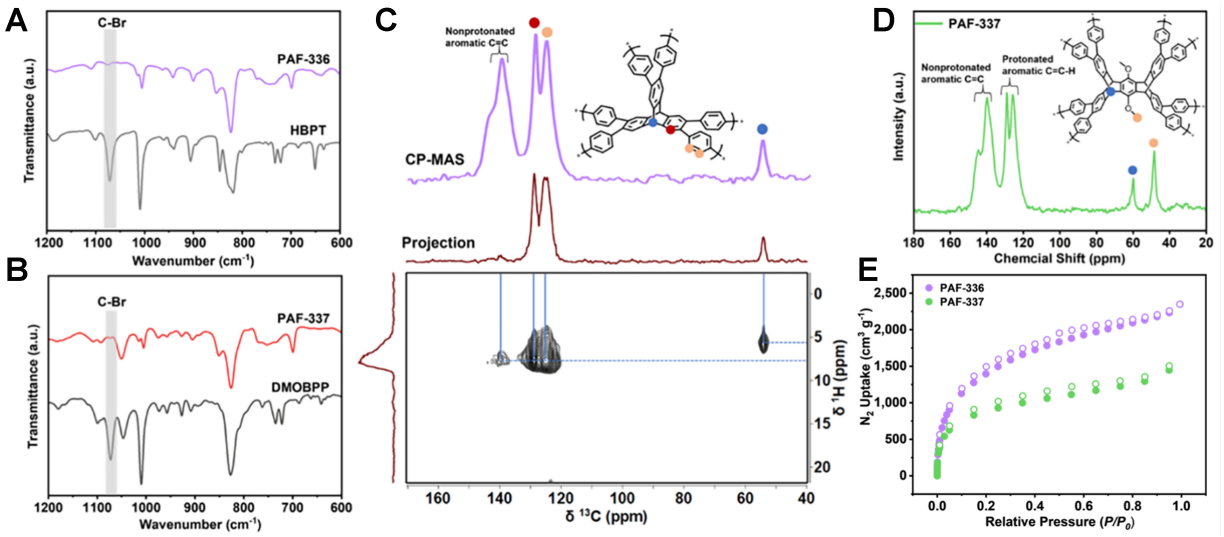

Figure 1. (A) FT-IR spectra of PAF-336 and HBPT; (B) FT-IR spectra of PAF-337 and DMOBPP; (C) Solid-state ^{13}C CP-MAS and 2D ^{1}H-^{13}C HETCOR NMR of PAF-336; (D) Solid-state ^{13}C CP-MAS NMR of PAF-337; (E) N_2 adsorption isotherms of PAF-336 and PAF-337. FT-IR: Fourier transform-infrared; HBPT: 2,3,6,7,14,15-hexa(4′-bromophenyl)triptycene; DMOBPP: 6,13-dimethoxy-2,3,9,10,18,19,24,25-octa(4′-bromophenyl)pentiptycene; CP-MAS: cross-polarization magic-angle spinning; HETCOR: heteronuclear correlation spectroscopy; NMR: nuclear magnetic resonance.

and PAF-337 revealed a distinct Br 3d peak in the monomers [Supplementary Figure 16], which disappeared after Ullmann coupling. This absence confirms the bromine removal during polymerization. The chemical structure of PAF-336 and PAF-337 was studied through the solid-state ^{13}C cross-polarization magic-angle spinning (CP-MAS) and 2D ^{1}H-^{13}C heteronuclear correlation spectroscopy (HETCOR) NMR. The solid-state ^{13}C NMR spectra of both PAFs [Figure 1C and D] show two types of carbon atoms: aromatic (125-145 ppm) and aliphatic (54 ppm for PAF-336; 48 and 60 ppm for PAF-337) carbon. Specifically, the 2D ^{1}H-^{13}C HETCOR NMR spectrum of PAF-336 shows different hydrogen atoms at 5.7 and 7.7 ppm, which reveal correlations with the aliphatic carbon atoms and aromatic carbon atoms. Strong correlations are exhibited as blue-, orange-, and red-labeled carbon, suggesting the direct bonding of hydrogen with tertiary carbon and aromatic carbon in the structure of PAF-336. The weak correlations of nonprotonated aromatic carbon atoms with hydrogen reveal long-distance contact. Combined analysis of FT-IR and solid-state NMR unequivocally confirmed the successful synthesis of both PAFs. Thermogravimetric analysis (TGA) under an air atmosphere revealed that PAF-336 exhibited higher thermal stability than PAF-337, with initial decomposition temperatures of ~400 and ~350 °C, respectively [Supplementary Figure 17]. Scanning electron microscopy (SEM) images revealed spherical PAF-336 and PAF-337 particles with sizes of 200-300 nm [Supplementary Figures 18 and 19]. Powder X-ray diffraction (PXRD) analysis confirmed the amorphous nature of both PAF-336 and PAF-337 [Supplementary Figure 20], consistent with previously reported PAFs[29,30]; this was further supported by transmission electron microscopy (TEM) images showing an absence of lattice fringes [Supplementary Figures 21 and 22].

As shown in Figure 1E, the nitrogen physisorption isotherms at 77 K reveal that both PAF-336 and PAF-337 exhibit Type I behavior according to the International Union of Pure and Applied Chemistry (IUPAC) classification. The BET surface areas were calculated to be ~5,210 and ~3,430 $m^2 \cdot g^{-1}$, respectively. The lower surface area of PAF-337 relative to PAF-336 is likely attributed to the higher molecular weight of the DMOBPP monomer compared to HBPT, which increases framework density. Additionally, the **bcu** topology involves denser packing of its constituent units, reducing internal voids and accessible surface area, thus lowering specific surface area. Conversely, the **acs** topology typically features a more open arrangement,

promoting greater porosity and surface accessibility and thereby enhancing specific surface area[46]. To confirm the reproducibility of PAF-336 synthesis, two independent batches showed nearly identical BET surface areas (~5,210 and ~5,180 $m^2 \cdot g^{-1}$, Supplementary Figure 23), demonstrating excellent synthetic consistency. Considering the scope of practical applications, PAF-336 must be compressed into gas storage tanks to minimize its volume. Therefore, we measured the nitrogen adsorption isotherms of PAF-336 after compression under a pressure of 10 MPa. As shown in Supplementary Figure 24, the BET surface area (5,140 $m^2 \cdot g^{-1}$) remains largely unchanged even in the compacted state, indicating that the porous structure is well preserved under high pressure.

The pore size distribution analysis of PAF-336 and PAF-337 - derived from quenched solid density functional theory (QSDFT) calculations employing a cylindrical pore approximation - exhibited a pronounced peak centered at approximately 2.4 and 2.1 nm, respectively [Supplementary Figure 25]. Quantitative analysis of nitrogen physisorption data at a relative pressure (P/P_0) of 0.95 revealed total pore volumes of 3.5 $cm^3 \cdot g^{-1}$ for PAF-336 and 2.5 $cm^3 \cdot g^{-1}$ for PAF-337. The experimentally calculated pore volume and pore size closely align with the theoretical predictions, with the exception of a slightly larger calculated pore size for PAF-337, which is likely attributable to framework flexibility. This demonstrates that computational simulations are a powerful tool for guiding the fabrication of highly porous polymers. Furthermore, the porosity of both PAFs was compared to other previously reported porous materials, including PAFs, COFs, hyper-cross-linked polymers (HCPs), and hydrogen-bonded organic frameworks (HOFs) [Supplementary Figure 26 and Supplementary Table 1]. Remarkably, the total pore volume of PAF-336 exceeds that of many porous materials with the same specific surface area. This significant observation is attributed to the unique pore structure of PAF-336. The BET surface area (derived from N_2 uptake at $P/P_0 < 0.2$) and the total pore volume (measured at $P/P_0 = 0.95$) are related yet distinct physical properties. The high pore volume at a comparable surface area indicates a significant portion of larger pores, likely originating from the framework's intrinsic architecture and potential defects, which contribute more to volume than to surface area[36]. These features - substantial pore volume together with high specific surface area - constitute critical parameters that significantly influence adsorption capacity and storage efficiency in gas storage applications[29,33]. This structural characteristic improves the adsorption capacity of porous materials by increasing adsorption sites and providing sufficient space. Furthermore, the chemical stability of PAF-336 was systematically assessed under harsh conditions, including exposure to 6 M concentrated HCl and 6 M NaOH for 72 h [Supplementary Figure 27]. The BET surface areas of the acid-treated and base-treated PAF-336 were 5,050 and 5,080 $m^2 \cdot g^{-1}$, respectively, corresponding to 97% and 98% retention of the pristine material's porosity. These results demonstrate the excellent physicochemical stability of PAF-336, indicating its suitability for long-term practical gas storage applications.

Hydrogen storage of PAF-336

Building on the analysis of pore architectures and H_2 storage performance criteria[34], PAF-336 emerges as a highly competitive candidate for H_2 storage applications, owing to its exceptionally high specific surface area, structural robustness, and facile synthetic route. In contrast, PAF-337 exhibits inherent synthetic limitations characterized by multistep synthesis, which impose potential challenges for practical application. Therefore, PAF-336 was selected for subsequent property investigation. High-pressure hydrogen adsorption measurements were conducted on PAF-336 at 77, 195, and 298 K to evaluate its H_2 storage performance. The total adsorption capacity and heat of adsorption were calculated according to the calculation methods section in the supporting information. The excess and total H_2 uptake values, as shown in Figure 2A, Supplementary Figure 28 and 29, reveal a total capacity of 14.7 wt% (35 $g \cdot L^{-1}$) at 77 K and 100 bar, placing PAF-336 among the top-performing materials [Figure 2B]. Upon increasing the pressure to 185 bar at 77 K, the uptake reaches 19.0 wt%. This exceptional performance is attributed to the material's high specific surface area and large pore volume. Gravimetric and volumetric capacity are key metrics for vehicle applications, yet

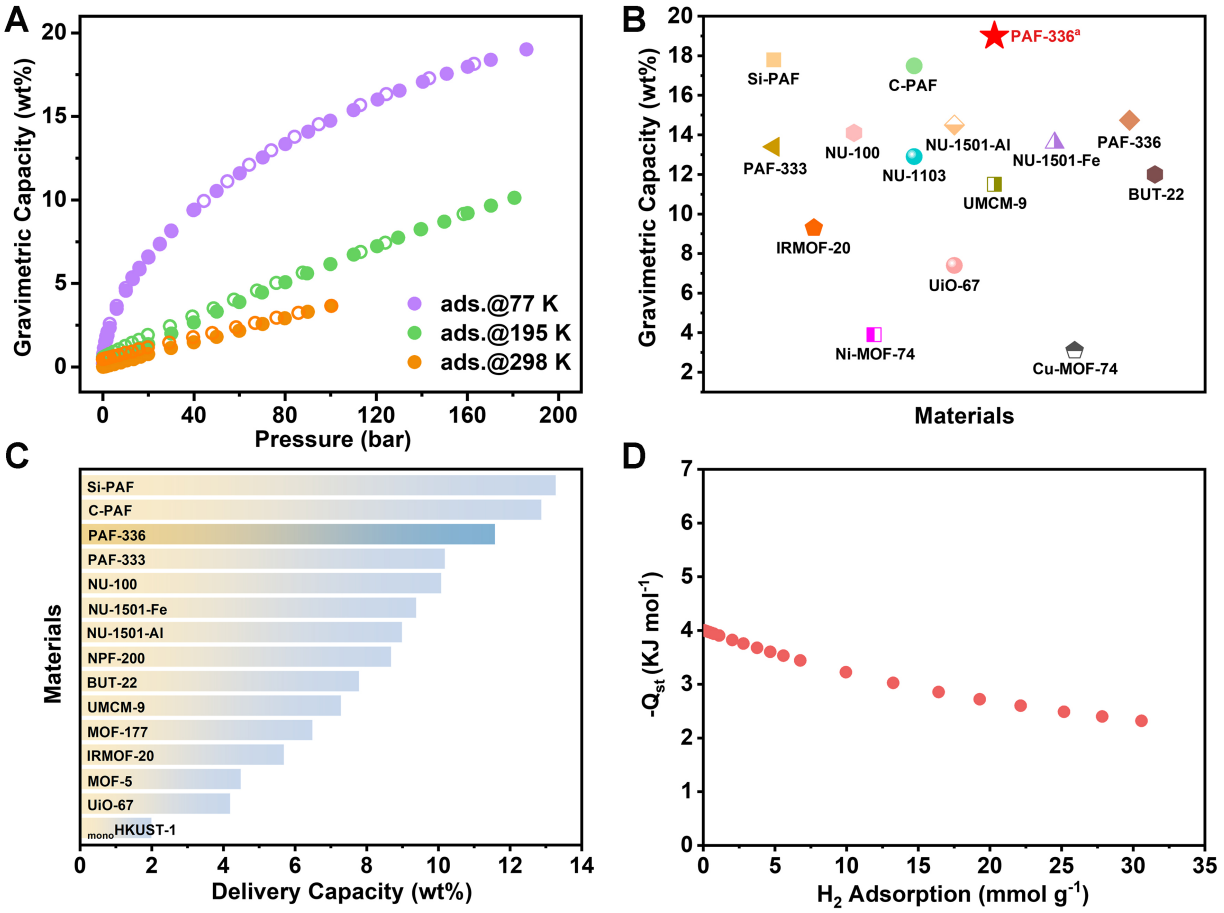

Figure 2. (A) Gravimetric hydrogen capacity of PAF-336 at various temperatures; (B) Comparison of gravimetric hydrogen capacity with several high-performing adsorbents [Supplementary Table 2]. PAF-336ª used the data tested at 185 bar, while PAF-336 used the data tested at 100 bar; (C) Comparison of gravimetric delivery capacities of hydrogen under PSA conditions (100 → 5 bar, 77 K) [Supplementary Table 2]; (D) The hydrogen Q_{st} for PAF-336. PSA: Pressure-swing adsorption.

balancing them is difficult. Materials with high volumetric capacity often have low gravimetric capacity due to density-volume trade-offs[47]. As shown in Supplementary Table 2 and literature[33], MOFs exceed 40 g·L^{-1} in volumetric capacity but face stability issues and lower gravimetric performance compared to porous organic polymers. Importantly, our material approaches the U.S. Department of Energy (DOE) volumetric target while maintaining high gravimetric capacity, achieving a balanced adsorption performance that directly contributes to vehicle lightweighting and reduced energy consumption[33].

The delivery capacity of H_2 storage materials is crucial for practical applications. In light-duty fuel cell vehicles, the minimum pressure needed to source hydrogen to the fuel cell module is 5 bar[33]. Therefore, we evaluated the hydrogen delivery capacity of PAF-336 by measuring its storage performance under 100 and 5 bar conditions [Supplementary Figure 30]. The delivery capacity under pressure-swing adsorption (PSA) conditions (100 → 5 bar, 77 K) was determined to be 11.6 wt% for PAF-336, ranking among the top reported porous materials and surpassed only by carbon-based PAF (C-PAF[33], 12.9 wt%) and silicon-based PAF (Si-PAF[33], 13.3 wt%) in gravimetric delivery capacity [Figure 2C]. For a more realistic approximation of practical conditions, the volumetric and deliverable capacities of PAF-336 were determined based on its tapped density to be 28.2 g·L^{-1} (77 K, 100 bar) and 22.3 g·L^{-1} (100 → 5 bar, 77 K), respectively [Supplementary Figure 31]. To further improve the hydrogen delivery capacity, a tank design for cryogenic condition H_2 storage has been proposed by the U.S. DOE center[48]. In this design, hydrogen adsorption

occurs at 77 K and 100 bar, while desorption occurs at a higher temperature and 5 bar. The delivery capacity under pressure-temperature swing adsorption (PTSA) conditions (77 K, 100 bar → 195 K, 5 bar) was determined to be 14.4 wt% for PAF-336 [Supplementary Figure 30].

The heat of adsorption is crucial for hydrogen adsorption and desorption because excessively high adsorption heat can be detrimental to hydrogen desorption[49]. The isosteric enthalpy of adsorption (Q_{st}) for hydrogen of PAF-336 was calculated using a virial equation to be -4.0 kJ·mol^{-1} at low pressure [Supplementary Figure 32 and Figure 2D], reaching the "optimal" value of -4.0 kJ·mol^{-1} for cryogenic condition H_2 storage[50]. PAF-336 releases less heat during hydrogen adsorption than other porous materials, indicating that it can adsorb and release hydrogen gas faster and more smoothly without significant heat exchange.

Methane storage of PAF-336

Methane has become an important transitional fuel for achieving carbon offset energy systems due to its large reserves, low cost, and low carbon-to-hydrogen (C/H) ratio[13,51]. However, storage tanks and multi-stage compression are still the majority of CH_4 storage technology at present, which is very energy-consuming and unsafe. Porous materials with ultra-high specific surface area provide new strategies for efficient and safe storage of methane. Here, high-pressure methane adsorption was tested to evaluate the adsorption capacity of PAF-336 [Figure 3A, Supplementary Figures 33 and 34]. At 100 bar, the total CH_4 uptake of PAF-336 was determined to be 0.536 g·g^{-1} (180 cm^3·cm^{-3}) at 298 K and 0.612 g·g^{-1} (206 cm^3·cm^{-3}) at 273 K, respectively. It is worth noting that the gravimetric adsorption capacity of PAF-336 at 100 bar exceeds the DOE target value (0.5 g·g^{-1}) at room temperature[10]. Compared to the state-of-the-art materials in previous reports [Figure 3B], the adsorption capacity of PAF-336 is higher than most porous materials, only slightly lower than that of PAF-333[49] (0.537 g·g^{-1}) and NU-1501-Al[47] (0.540 g·g^{-1}). Moreover, PAF-336 maintained the high BET surface area (5,030 m^2·g^{-1}) after high-pressure methane adsorption and desorption tests [Supplementary Figure 35], confirming its stability in the CH_4 storage process.

The delivery capacity and storage capacity of methane determine the actual driving distance of adsorbed natural gas (ANG) vehicles, as the minimum inlet pressure of the engine requires 5 bar[18]. As shown in Figure 3C, the delivery capacity (100 → 5 bar) calculated for PAF-336 was 0.50 g·g^{-1} at 298 K, ranking among the top-performing reported porous organic materials, level with NU-1501-Al[47]. For a more realistic approximation of practical conditions, the volumetric and deliverable capacities of PAF-336 were determined based on its tapped density to be 103 g·L^{-1} (298 K, 100 bar) and 96 g·L^{-1} (100 → 5 bar, 298 K), respectively [Supplementary Figure 36]. Moreover, the deliverable methane capacity of PAF-336 was evaluated at 298 K between 5 and 80 bar. As shown in Supplementary Table 3, PAF-336 exhibits a high deliverable capacity of 0.42 g·g^{-1} under these conditions. Although slightly lower than that of NU-1501-Al (0.44 g·g^{-1}) under similar conditions, this value remains highly competitive among advanced porous materials, demonstrating the promising potential of PAF-336 for CH_4 storage applications. Cyclical stability is crucial for industrial CH_4 storage applications. The material demonstrates robust performance, as evidenced by CH_4 capacity over three adsorption-desorption cycles [Supplementary Figure 37]. To further investigate the methane-adsorbent interactions, the Q_{st} was calculated from adsorption isotherms of methane measured at 273 and 298 K, employing the virial equation [Supplementary Figure 38]. Figure 3D shows that PAF-336 has a low Q_{st} value (10.2 kJ·mol^{-1}) at minimal loading, lower than most benchmark porous materials under similar conditions, which will reduce the CH_4 uptake at low pressure (5 bar)[18,47,49,52]. As evidenced by the preceding investigation, the superior working capacity of PAF-336 arises from the synergistic interplay between its high pore volume and low adsorption heat. High pore volume enhances methane adsorption capacity by providing ample storage space[53-55], while low adsorption heat facilitates rapid desorption by overcoming the small energy barrier[18].

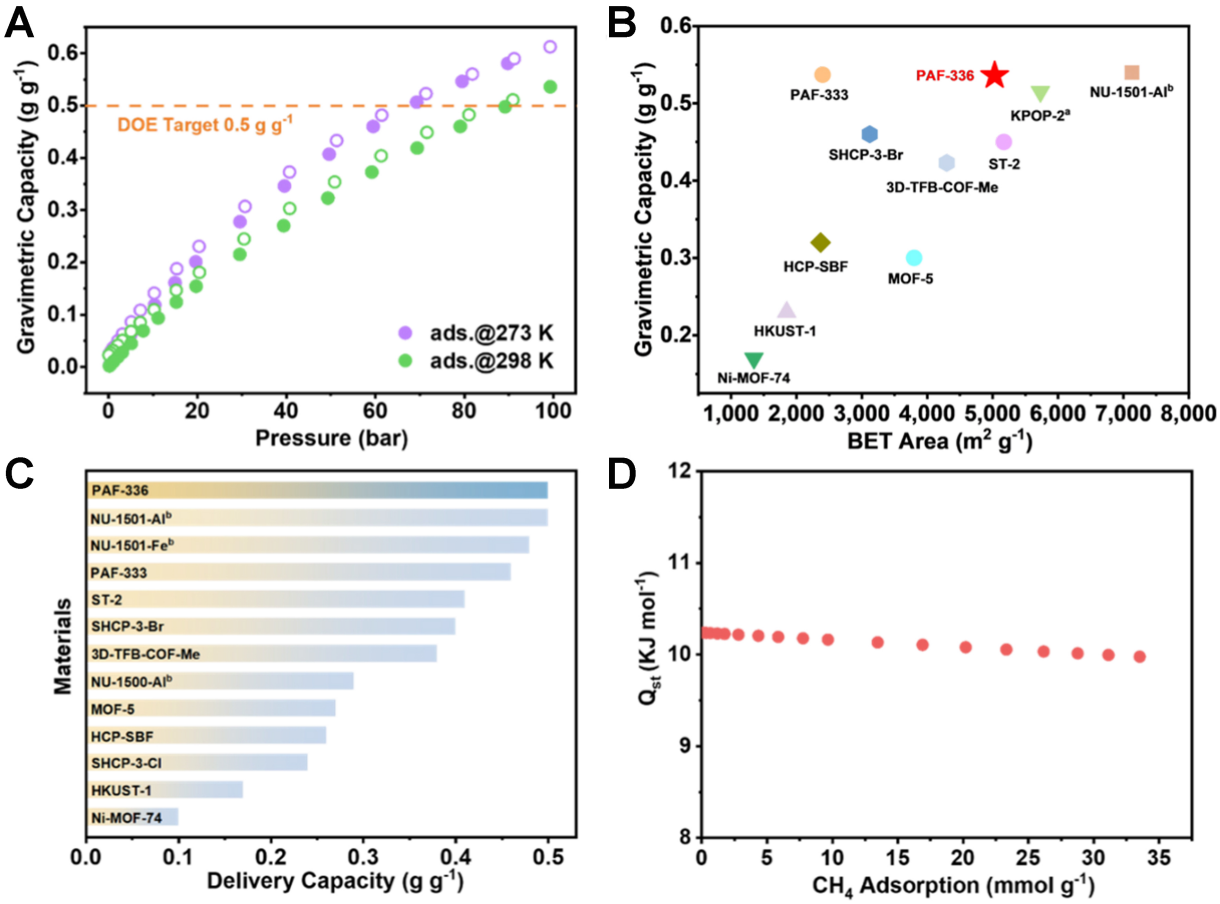

Figure 3. (A) The total methane capacity of PAF-336 at 298 and 273 K; (B) Comparison of the total methane capacity and BET surface areas with previously reported highly porous materials [Supplementary Table 3]; (C) Comparison of the gravimetric delivery capacity of methane with some of the high performing adsorbents (100 ⟶ 5 bar, 298 K, Supplementary Table 3); (D) The methane Q_{st} for PAF-336. BET: Brunauer-Emmett-Teller; DOE: U.S. Department of Energy.

CONCLUSIONS

In summary, we have rationally designed and successfully synthesized two porous aromatic frameworks, PAF-336 and PAF-337, both featuring high specific surface areas and large pore volumes. Remarkably, PAF-336 delivers exceptional gravimetric H_2 and CH_4 storage performance, ranking among the highest levels ever reported for porous organic materials. This work demonstrates the powerful capability of rational framework engineering in optimizing gas storage properties, and our ongoing efforts are focused on developing innovative building blocks to further advance the gas storage performance of porous organic frameworks.

DECLARATIONS

Authors' contributions

Conception: Jia, J.; Su, B. L.; Zhu, G.

Planned the study, analyzed the data, and wrote the manuscript: Cui, L.; Zhang, M.; Wang, Q.; Jia, J.; Bian, Z.

Synthesis and analytical discussions: Cui, L.; Zhang, M.; Wang, Q.; Wang, Z.; Liu, J.

NMR and TEM characterization: Feng, D.; Lin, L.

Availability of data and materials

The raw data supporting the findings of this study are available within this Article and its Supplementary Materials. Further data can be available from the corresponding authors upon reasonable request.

AI and AI-assisted tools statement

Not applicable.

Financial support and sponsorship

We thank Beishide Instrument Technology (Beijing) Co., Ltd. for providing the high-pressure gas adsorption measurements. Financial support from the National Key R&D Program of China (2022YFB3805902, 2022YFB3805900), the National Natural Science Foundation of China (Grant Nos. 22131004, U21A20330), the "111" project (B18012), and the Fundamental Research Funds for the Central Universities (2412024QD012) is gratefully acknowledged.

Conflicts of interest

Su, B. L. is Editor-in-Chief of the journal *Chemical Synthesis*. Zhu, G. is Executive Editor-in-Chief of the journal *Chemical Synthesis*. Su, B. L. and Zhu, G. were not involved in any steps of the editorial process, notably including reviewers' selection, manuscript handling, or decision-making. Liu, J. is affiliated with Analysis Lab, Beishide Instrument Technology (Beijing) Co., Ltd. The other authors declare that there are no conflicts of interest.

Ethical approval and consent to participate

Not applicable.

Consent for publication

Not applicable.

Supplementary Materials

Supplementary Materials

REFERENCES

1. Zhou, Z.; Ma, T.; Zhang, H.; et al. Carbon dioxide capture from open air using covalent organic frameworks. *Nature* **2024**, *635*, 96-101. DOI PubMed
2. Zhu, Z.; Tsai, H.; Parker, S. T.; et al. High-capacity, cooperative CO_2 capture in a diamine-appended metal-organic framework through a combined chemisorptive and physisorptive mechanism. *J. Am. Chem. Soc.* **2024**, *146*, 6072-83. DOI PubMed PMC
3. Morris, R. E.; Wheatley, P. S. Gas storage in nanoporous materials. *Angew. Chem. Int. Ed. Engl.* **2008**, *47*, 4966-81. DOI PubMed
4. Wang, Z.; Zhang, Y.; Jiang, L.; et al. Post-modified porous aromatic frameworks for carbon dioxide capture. *Chem. Synth.* **2024**, *4*, 40. DOI
5. Wang, X.; Alzayer, M.; Shih, A. J.; et al. Tailoring hydrophobicity and pore environment in physisorbents for improved carbon dioxide capture under high humidity. *J. Am. Chem. Soc.* **2024**, *146*, 3943-54. DOI PubMed
6. Li, H.; Zhou, Z.; Ma, T.; et al. Bonding of polyethylenimine in covalent organic frameworks for CO_2 capture from air. *J. Am. Chem. Soc.* **2024**, *146*, 35486-92. DOI PubMed
7. Abelson, P. H. Limiting atmospheric CO_2. *Science* **2000**, *289*, 1293. DOI
8. Furukawa, H.; Yaghi, O. M. Storage of hydrogen, methane, and carbon dioxide in highly porous covalent organic frameworks for clean energy applications. *J. Am. Chem. Soc.* **2009**, *131*, 8875-83. DOI PubMed
9. Breunig, H.; Rosner, F.; Saqline, S.; et al. Achieving gigawatt-scale green hydrogen production and seasonal storage at industrial locations across the U.S. *Nat. Commun.* **2024**, *15*, 9049. DOI PubMed PMC
10. Yin, Y.; Zhang, Y.; Zhou, X. et. al. Ultrahigh-surface area covalent organic frameworks for methane adsorption. *Science* **2024**, *386*, 693-96. DOI PubMed
11. Hwang, H. T.; Varma, A. Hydrogen storage for fuel cell vehicles. *Curr. Opin. Chem. Eng.* **2014**, *5*, 42-8. DOI
12. Zhang, C.; Cao, X.; Bujlo, P.; et al. Review on the safety analysis and protection strategies of fast filling hydrogen storage system for fuel cell vehicle application. *J. Energy. Storage.* **2022**, *45*, 103451. DOI
13. Kumar, K. V.; Preuss, K.; Titirici, M. M.; Rodríguez-Reinoso, F. Nanoporous materials for the onboard storage of natural gas. *Chem. Rev.* **2017**, *117*, 1796-825. DOI PubMed

14. He, Y.; Chen, F.; Li, B.; Qian, G.; Zhou, W.; Chen, B. Porous metal–organic frameworks for fuel storage. *Coord. Chem. Rev.* **2018**, *373*, 167-98. DOI
15. Saha, D.; Grappe, H. A.; Chakraborty, A.; Orkoulas, G. Postextraction separation, on-board storage, and catalytic conversion of methane in natural gas: a review. *Chem. Rev.* **2016**, *116*, 11436-99. DOI PubMed
16. He, Y.; Zhou, W.; Qian, G.; Chen, B. Methane storage in metal-organic frameworks. *Chem. Soc. Rev.* **2014**, *43*, 5657-78. DOI PubMed
17. Wang, Y.; Xue, Y.; Züttel, A. Nanoscale engineering of solid-state materials for boosting hydrogen storage. *Chem. Soc. Rev.* **2024**, *53*, 972-1003. DOI PubMed
18. Makal, T. A.; Li, J. R.; Lu, W.; Zhou, H. C. Methane storage in advanced porous materials. *Chem. Soc. Rev.* **2012**, *41*, 7761-79. DOI PubMed
19. Zhang, R.; Daglar, H.; Tang, C.; et al. Balancing volumetric and gravimetric capacity for hydrogen in supramolecular crystals. *Nat. Chem.* **2024**, *16*, 1982-8. DOI PubMed
20. Yu, B.; Tao, Y.; Yao, X.; et al. Single-crystalline 3D covalent organic frameworks with exceptionally high specific surface areas and gas storage capacities. *J. Am. Chem. Soc.* **2024**, *146*, 28932-40. DOI PubMed
21. Tian, Y.; Zhu, G. Porous aromatic frameworks (PAFs). *Chem. Rev.* **2020**, *120*, 8934-86. DOI PubMed
22. Luo, D.; Li, M.; Ma, Q.; et al. Porous organic polymers for Li-chemistry-based batteries: functionalities and characterization studies. *Chem. Soc. Rev.* **2022**, *51*, 2917-38. DOI PubMed
23. Ma, T.; Zhou, Y.; Diercks, C. S.; et al. Catenated covalent organic frameworks constructed from polyhedra. *Nat. Synth.* **2023**, *2*, 286-95. DOI
24. Lee, J. M.; Cooper, A. I. Advances in conjugated microporous polymers. *Chem. Rev.* **2020**, *120*, 2171-214. DOI PubMed PMC
25. Tan, L.; Tan, B. Hypercrosslinked porous polymer materials: design, synthesis, and applications. *Chem. Soc. Rev.* **2017**, *46*, 3322-56. DOI
26. Asif, M. B.; Kim, S.; Nguyen, T. S.; Mahmood, J.; Yavuz, C. T. Covalent organic framework membranes and water treatment. *J. Am. Chem. Soc.* **2024**, *146*, 3567-84. DOI PubMed PMC
27. Sun, T.; Liang, Y.; Luo, W.; Zhang, L.; Cao, X.; Xu, Y. A general strategy for kilogram-scale preparation of highly crystal-line covalent triazine frameworks. *Angew. Chem. Int. Ed. Engl.* **2022**, *61*, e202203327. DOI PubMed
28. Ben, T.; Ren, H.; Ma, S.; et al. Targeted synthesis of a porous aromatic framework with high stability and exceptionally high surface area. *Angew. Chem. Int. Ed. Engl.* **2009**, *48*, 9457-60. DOI PubMed
29. Yuan, D.; Lu, W.; Zhao, D.; Zhou, H. C. Highly stable porous polymer networks with exceptionally high gas-uptake capacities. *Adv. Mater.* **2011**, *23*, 3723-5. DOI PubMed
30. Ben, T.; Pei, C.; Zhang, D.; et al. Gas storage in porous aromatic frameworks (PAFs). *Energy. Environ. Sci.* **2011**, *4*, 3991. DOI
31. Jia, J.; Chen, Z.; Jiang, H.; et al. Extremely hydrophobic POPs to access highly porous storage media and capturing agent for organic vapors. *Chem* **2019**, *5*, 180-91. DOI
32. Li, M.; Ren, H.; Sun, F.; et al. Construction of porous aromatic frameworks with exceptional porosity via building unit engineering. *Adv. Mater.* **2018**, *30*, e1804169. DOI PubMed
33. Kim, D. W.; Chen, Y.; Kim, H.; et al. High hydrogen storage in trigonal prismatic monomer-based highly porous aromatic frameworks. *Adv. Mater.* **2024**, *36*, e2401739. DOI PubMed
34. Chen, Z.; Kirlikovali, K. O.; Idrees, K. B.; Wasson, M. C.; Farha, O. K. Porous materials for hydrogen storage. *Chem* **2022**, *8*, 693-716. DOI
35. Zhou, S.; Qiu, T.; Wang, H.; et al. Flexible porous organic polymers constructed using $C(sp^3)$-$C(sp^3)$ coupling reactions and their high methane-storage capacity. *Chem. Sci.* **2024**, *15*, 10830-7. DOI PubMed PMC
36. Li, H.; Chen, F.; Guan, X.; et al. Three-dimensional triptycene-based covalent organic frameworks with ceq or acs topology. *J. Am. Chem. Soc.* **2021**, *143*, 2654-9. DOI PubMed
37. Gong, W.; Gao, P.; Gao, Y.; et al. Modulator-directed counterintuitive catenation control for crafting highly porous and robust metal-organic frameworks with record high SO_2 uptake capacity. *J. Am. Chem. Soc.* **2024**, *146*, 31807-15. DOI PubMed
38. Zhu, Q.; Wang, X.; Clowes, R.; et al. 3D cage COFs: a dynamic three-dimensional covalent organic framework with high-connectivity organic cage nodes. *J. Am. Chem. Soc.* **2020**, *142*, 16842-8. DOI PubMed PMC
39. Yang, Q.; Chen, K.; Schoedel, A.; Wojtas, L.; Perry Iv, J. J.; Zaworotko, M. J. Network diversity through two-step crystal engineering of a decorated 6-connected primary molecular building block. *CrystEngComm* **2016**, *18*, 8578-81. DOI
40. Zhou, J.; Zhang, Z.; Xu, L.; et al. Mixed-ligand strategy affording two 6-connected 3-fold interpenetrated metal-organic frameworks with binuclear CoII2/NiII2 subunits: synthesis, crystal structures and magnetic properties. *Inorg. Chem. Commun.* **2020**, *111*, 107624. DOI
41. Li, W.; Probert, M. R.; Kosa, M.; et al. Negative linear compressibility of a metal-organic framework. *J. Am. Chem. Soc.* **2012**, *134*, 11940-3. DOI PubMed

42. Yin, Y.; Zhang, Y.; Zhou, X.; et al. Single-crystal three-dimensional covalent organic framework constructed from 6-connected triangular prism node. *J. Am. Chem. Soc.* **2023**, *145*, 22329-34. DOI PubMed
43. Zhao, Y.; Irie, T.; Wen, D.; et al. Highly selective separation of benzene/cyclohexane by three-dimensional covalent organic framework with 8,8-connected bcu net topology. *ACS. Materials. Lett.* **2024**, *6*, 3063-70. DOI
44. Alezi, D.; Belmabkhout, Y.; Suyetin, M.; et al. MOF crystal chemistry paving the way to gas storage needs: aluminum-based soc-MOF for CH_4, O_2, and CO_2 storage. *J. Am. Chem. Soc.* **2015**, *137*, 13308-18. DOI PubMed PMC
45. Liu, W.; Wu, E.; Yu, B.; et al. Reticular synthesis of metal-organic frameworks by 8-connected quadrangular prism ligands for water harvesting. *Angew. Chem. Int. Ed. Engl.* **2023**, *62*, e202305144. DOI PubMed
46. Chen, F.; Zheng, H.; Yusran, Y.; Li, H.; Qiu, S.; Fang, Q. Exploring high-connectivity three-dimensional covalent organic frameworks: topologies, structures, and emerging applications. *Chem. Soc. Rev.* **2025**, *54*, 484-514. DOI PubMed
47. Chen, Z.; Li, P.; Anderson, R.; et al. Balancing volumetric and gravimetric uptake in highly porous materials for clean energy. *Science* **2020**, *368*, 297-303. DOI PubMed
48. Parks, G.; Boyd, R.; Cornish, J.; Remick, R. Hydrogen station compression, storage, and dispensing technical status and costs. 2014. https://docs.nrel.gov/docs/fy14osti/58564.pdf. (accessed 31 Dec 2025).
49. Wang, Z.; Jiang, L.; Jia, J.; Zhu, G. Targeted synthesis of interpenetration-free mesoporous aromatic frameworks by manipulating catalysts as templates. *Angew. Chem. Int. Ed. Engl.* **2025**, *64*, e202420746. DOI PubMed
50. Gómez-Gualdrón, D. A.; Colón, Y. J.; Zhang, X.; et al. Evaluating topologically diverse metal–organic frameworks for cryo-adsorbed hydrogen storage. *Energy. Environ. Sci.* **2016**, *9*, 3279-89. DOI
51. Budzianowski, W. M.; Brodacka, M. Biomethane storage: evaluation of technologies, end uses, business models, and sustainability. *Energy. Convers. Manag.* **2017**, *141*, 254-73. DOI
52. Yang, S.; Zhong, Z.; Hu, J.; Wang, X.; Tan, B. Dibromomethane knitted highly porous hyper-cross-linked polymers for efficient high-pressure methane storage. *Adv. Mater.* **2024**, *36*, e2307579. DOI PubMed
53. Tan, J.; Tao, Y.; Zhang, X.; et al. Control over interpenetration for boosting methane storage capacity in metal–organic frameworks. *J. Mater. Chem. A.* **2021**, *9*, 24857-62. DOI
54. Froudas, K. G.; Vassaki, M.; Papadopoulos, K.; et al. Expanding the reticular chemistry building block library toward highly connected nets: ultraporous MOFs based on 18-connected ternary, trigonal prismatic superpolyhedra. *J. Am. Chem. Soc.* **2024**, *146*, 8961-70. DOI PubMed PMC
55. Li, B.; Wen, H.; Zhou, W.; Xu, J.; Chen, B. Porous metal-organic frameworks: promising materials for methane storage. *Chem* **2016**, *1*, 557-80. DOI

Jiangtao Jia

Professor Jiangtao Jia (Northeast Normal University) obtained his doctoral degree from Jilin University in 2014 under the supervision of Professor Guangshan Zhu. He previously worked as a postdoctoral researcher and research scientist in the groups of Professor Kimoon Kim at POSTECH in South Korea and Professor Eddaoudi at KAUST in Saudi Arabia. He has published over 50 articles in journals such as *Nature*, *Science*, *Chem*, *Matter*, *J. Am. Chem. Soc.*, and *Angew. Chem. Int. Ed.* His current research focuses on the design, synthesis, and functional development of PAFs and metal-carbon bond MOFs.

Zheng Bian

Zheng Bian is a Professor at the School of Chemistry, Northeast Normal University. His research interests include molecular self-assembly and the synthesis and application of porous materials. He has led and participated in multiple national research projects and has published over 20 papers as corresponding author in journals such as *Angew. Chem. Int. Ed.*, *Chem. Sci.*, *Chem.–Eur. J.*, *Chem. Commun.*, *J. Mater. Chem. A*, and *Soft Matter*.

Bao-Lian Su

Bao-Lian Su established the Laboratory of Inorganic Materials Chemistry (CMI) at the University of Namur, Belgium, in 1995. He is a Full Professor, Member of the European Academy of Sciences, Member of the Royal Academy of Belgium, Honorary Fellow of the Chinese Chemical Society, Fellow of the Royal Society of Chemistry (UK), and Life Member of Clare Hall College, University of Cambridge. He also serves as a "Strategy Scientist" at Wuhan University of Technology, China. His research interests include the synthesis, property characterization, and molecular engineering of organized, hierarchically porous materials and bio-organisms for applications in artificial photosynthesis, (photo)catalysis, energy conversion and storage, biotechnology, cell therapy, and biomedical science.

Guangshan Zhu

Professor Guangshan Zhu (Northeast Normal University) is a member of the Discipline Evaluation Group of the Subject Academic Degrees Committee of the State Council and a recipient of the National Science Fund for Distinguished Young Scholars. Professor Zhu has long been engaged in the synthesis of new porous materials and the development of their potential applications. He pioneered the research field of porous organic molecular sieves - porous aromatic frameworks (PAFs) - and has achieved leading results in the field of porous membrane materials.